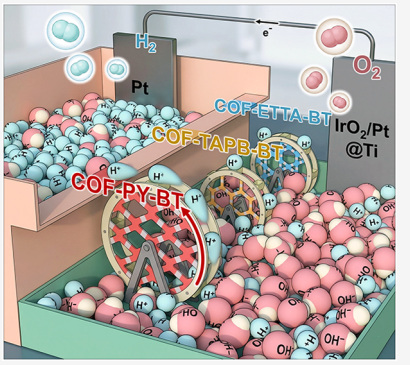
JACS
JOURNAL OF THE AMERICAN CHEMICAL SOCIETY
pubs.acs.org/JACS
Article

Light-Driven Active Separation Sustains a Transmembrane Proton-Activity Difference for Electrochemical Microenvironment Regulation

Zhuozhi Lai, Zhiwei Xing, Yongxin Ge, Jiaming Yi, Sai Wang, Ruotian Chen, Shengqian Ma, and Qi Sun*

Cite This: J. Am. Chem. Soc. 2026, 148, 38932−38940
Read Online
ACCESS | Metrics & More | Article Recommendations | Supporting Information

ABSTRACT: Electrochemical water technologies often require spatially distinct proton activities, yet passive membranes allow these microenvironments to equilibrate. Here we construct a topology-defined series of donor−acceptor covalent organic framework (COF) membranes with rhombic, honeycomb, and kagome lattices and establish a connection between local photoinduced responses and membrane-scale active ion transport. Among them, rhombic COF-PY-BT exhibits the strongest local photoresponse and the largest light-induced transmembrane bias under one-sided illumination. Crossed-control experiments establish that the direction of the macroscopic response follows the illumination direction, while periodic Berry-phase calculations reveal framework-dependent retention and cancellation of dipolar components. The resulting transmembrane bias counteracts proton back-diffusion and enables uphill proton transport, helping sustain a bulk ΔpH > 4 between near-neutral anodic and acidic cathodic compartments. When integrated as an active separator in a two-compartment electrolysis cell, COF-PY-BT lowers the apparent full-cell voltage by approximately 45% under dilute conditions and improves voltage stability. These results establish light-driven active membrane regulation as a strategy for sustaining nonequilibrium proton environments during electrochemical operation.



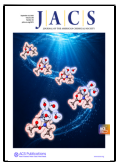
1. INTRODUCTION

Aqueous electrochemical technologies increasingly rely on the precise regulation of local reaction environments.[1−3] In many coupled electrochemical processes, including water splitting, the two half-reactions favor distinct proton activities. The hydrogen evolution reaction (HER) is generally accelerated in acidic media, whereas the oxygen evolution reaction (OER) is often more favorable under near-neutral or alkaline conditions.[4−6] Maintaining such distinct environments could enable the anodic and cathodic reactions to be optimized more independently. However, conventional electrolyzers typically employ passive ion-exchange membranes and bulk electrolytes, through which proton and ion distributions continuously relax by diffusion. This equilibration progressively erodes the desired chemical asymmetry, narrows the accessible operating window for catalysts, and introduces additional energetic penalties.[7,8] A central challenge is therefore not merely to separate electrolytes or conduct charge, but to actively sustain nonequilibrium proton distributions across hydrated membrane interfaces against continuous back-diffusion.

Biological membranes address an analogous challenge through active ion pumping, in which chemical or optical energy is converted into directional ion transport to sustain electrochemical gradients across membrane interfaces (Figure 1a).[9−12] This principle has inspired artificial systems capable of light-driven proton or ion transport, including photoresponsive carriers in liquid membranes and nanofluidic solid membranes.[13,14] Yet translating active pumping into solid-state separators for aqueous electrochemical operation remains challenging.[15−19] In water, proton and ion gradients are continuously dissipated by diffusion, requiring an active driving force capable of operating against spontaneous equilibration.[20−22] Donor−acceptor structures can promote photoinduced charge separation, but a local photoresponse does not necessarily translate into a net electrical bias across an extended membrane.[23−28] How molecular-scale photoinduced charge separation, periodic framework organization, and asymmetric excitation collectively contribute to a directional transmembrane electrical response therefore remains an important unresolved question. In crystalline membranes, framework organization may modulate the retention or cancellation of dipolar components,[29−34] while one-sided illumination provides a spatially asymmetric excitation condition across the membrane thickness.

Covalent organic frameworks (COFs) provide a programmable platform for addressing this question because their

Received: May 27, 2026
Revised: August 26, 2026
Accepted: August 27, 2026
Published: September 1, 2026



Downloaded from pubs.acs.org/jacsat/article-pdf/148/36/38932/6810152/jacs.6c10380.pdf by UNIV OF NORTH TEXAS user on 26 September 2026

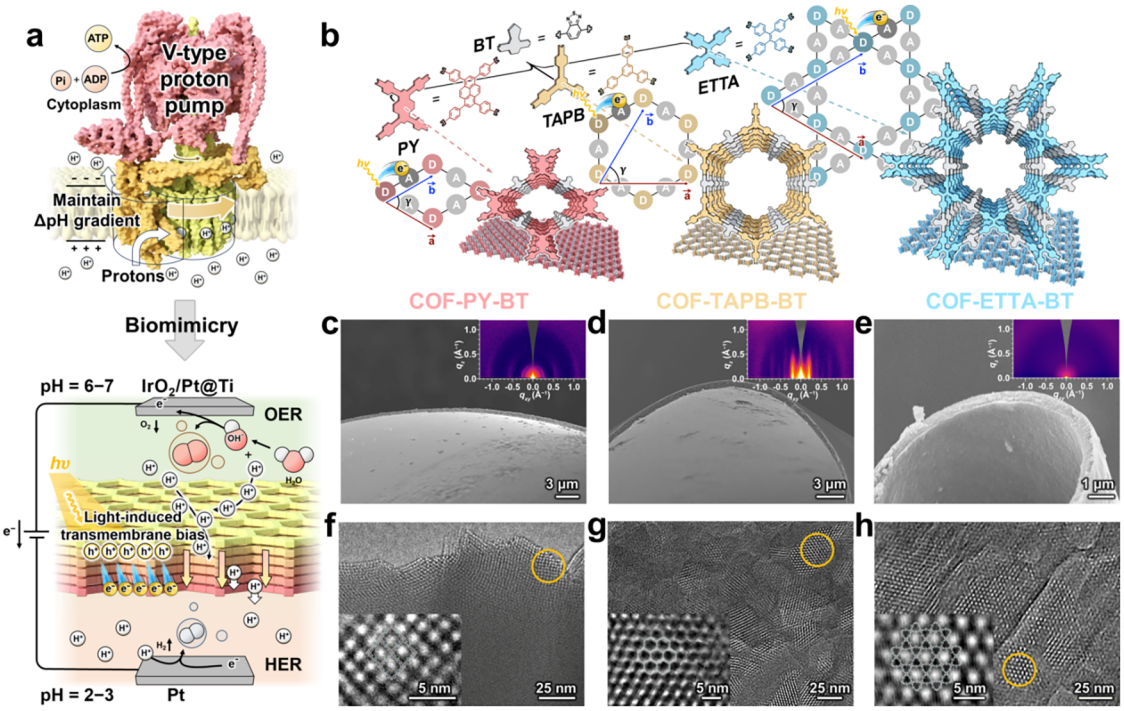


Figure 1. Biomimetic concept and topology-defined COF membranes. (a) Schematic comparison of a biological V-type proton pump and a light-responsive solid-state separator. In the artificial system, a light-induced transmembrane bias suppresses proton back-diffusion and helps maintain distinct near-neutral anodic and acidic cathodic environments. (b) Topology-defined donor–acceptor COF membranes with distinct framework symmetries constructed using the common BT acceptor and PY, TAPB, or ETTA donors to form rhombic COF-PY-BT, honeycomb COF-TAPB-BT, and kagome COF-ETTA-BT, respectively. (c–e) Cross-sectional SEM images of COF-PY-BT, COF-TAPB-BT, and COF-ETTA-BT membranes. Insets show the corresponding 2D-GIWAXS patterns. (f–h) HR-TEM images of COF-PY-BT, COF-TAPB-BT, and COF-ETTA-BT. Insets show magnified regions marked by orange circles.

molecular composition, pore architecture, and lattice topology can be controlled with high precision in crystalline membranes.[35−50] Here, we construct a topology-defined series of donor–acceptor COF membranes with rhombic, honeycomb, and kagome lattices to investigate light-driven transmembrane ion transport. Among them, rhombic COF-PY-BT exhibits a pronounced local photoresponse together with the largest light-induced transmembrane bias under one-sided illumination, enabling uphill proton transport against back-diffusion and the maintenance of distinct proton environments across the membrane. Integration of the active membrane into a two-compartment electrochemical system further demonstrates that such light-driven transport can regulate non-equilibrium proton distributions under operating conditions. This work establishes active membrane regulation as a strategy for controlling electrochemical microenvironments in water.

2. RESULTS AND DISCUSSION

2.1. Topology-Defined Framework Membranes for Directional Ion Transport

To establish a structurally comparable membrane platform, we combined a common benzothiadiazole (BT) acceptor and imine linkage with three geometrically distinct amine donors: 4,4′,4″,4‴-(pyrene-1,3,6,8-tetrayl)tetraaniline (PY), 1,3,5-tris-(4-aminophenyl)benzene (TAPB), and 4,4′,4″,4‴-(ethene-1,1,2,2-tetrayl)tetraaniline (ETTA). This design preserves a shared acceptor and linkage chemistry while varying donor geometry and network topology, yielding rhombic COF-PY-BT, honeycomb COF-TAPB-BT, and kagome COF-ETTA-BT, respectively (Figure 1b and Schemes S1–S3). Continuous free-standing membranes were prepared by interfacial polymerization, with representative atomic force microscopy (AFM) step heights of 822, 866, and 831 nm for COF-PY-BT, COF-TAPB-BT, and COF-ETTA-BT, respectively, providing comparable membrane thicknesses for subsequent transport measurements (Figures 1c–e and S1–S3).

Structural analyses confirmed that all three membranes are highly crystalline imine-linked frameworks with long-range order, as supported by high-resolution transmission electron microscopy (HR-TEM) and Pawley-refined X-ray diffraction (Figures 1f–h and S4–S8 and Tables S1–S3). The corresponding structural models exhibit distinct network topologies and lattice symmetries, represented by the proposed *P*2*mm*, $P\bar{6}$, and *P*6 structures derived from PXRD/Pawley analyses and structural modelling. Second-harmonic generation (SHG) measurements provided complementary characterization of their effective second-order nonlinear optical responses. Under identical 1030 nm femtosecond-laser excitation conditions, COF-PY-BT exhibited the strongest SHG response, with a pronounced signal at approximately 515 nm, whereas COF-TAPB-BT and COF-ETTA-BT showed substantially weaker responses (Figure S9).

At the membrane scale, however, all three frameworks share several features relevant to ion transport. Two-dimensional grazing-incidence wide-angle X-ray scattering (2D-GIWAXS) patterns and the corresponding line-cut analyses indicate preferential framework orientation consistent with predominantly through-plane channel alignment in all three membranes (Figures 1c–e, insets, and S10). N_2 sorption measurements further confirm permanent porosity, with Brunauer–

Downloaded from pubs.acs.org/jacsat/article-pdf/148/36/38932/6810152/jacs.6c10380.pdf by UNIV OF NORTH TEXAS user on 26 September 2026

https://doi.org/10.1021/jacs.6c10380
J. Am. Chem. Soc. 2026, 148, 38932−38940

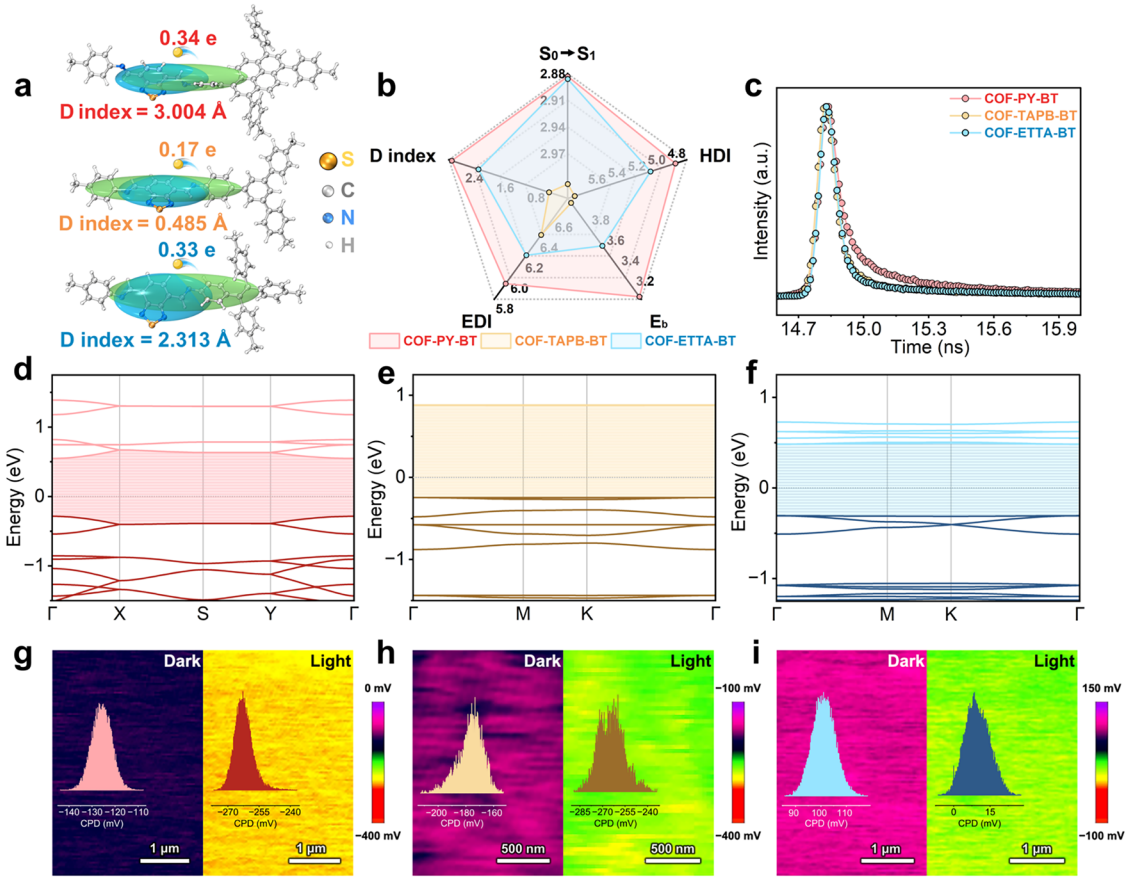


Figure 2. Local photoinduced charge separation and surface photovoltage in COF membranes. (a) Calculated excited-state charge-density difference maps for donor−acceptor repeating units derived from COF-PY-BT, COF-TAPB-BT, and COF-ETTA-BT (top to bottom). Blue and green indicate electron accumulation and depletion, respectively; the D index denotes the electron−hole centroid separation. (b) Radar plot comparing the D index, hole and electron delocalization indices (HDI and EDI), exciton binding energy (E_b), and the $S_0 \rightarrow S_1$ transition. (c) Time-resolved photoluminescence decays measured under low excitation fluence. (d−f) Calculated electronic band structures of COF-PY-BT, COF-TAPB-BT, and COF-ETTA-BT, respectively. The shaded regions indicate the relative energy ranges of the valence and conduction bands. (g−i) KPFM surface-potential maps of the three membranes acquired in the dark and under illumination. Insets show the corresponding contact potential difference (CPD) distributions.

Emmett−Teller (BET) surface areas of 1450, 879, and 975 m^2 g^{-1} for COF-PY-BT, COF-TAPB-BT, and COF-ETTA-BT, respectively, together with pore-size distributions consistent with their designed structures (Figure S11).

2.2. Local Photoinduced Charge Separation and Surface Photovoltage

We first compared the local photoinduced responses of the three frameworks. All three membranes absorb strongly across the xenon-lamp emission range (Figure S12), providing a common optical basis for comparing their excited-state behavior. Temperature-dependent photoluminescence (PL) measurements revealed distinct excited-state relaxation characteristics. COF-PY-BT and COF-TAPB-BT showed monotonic PL quenching from 75 to 290 K, consistent with thermally activated nonradiative recombination, whereas COF-ETTA-BT exhibited an inverse temperature dependence, indicating a different excited-state relaxation pathway (Figure S13).[51,52] Further analysis yielded a lower exciton binding energy for COF-PY-BT (60.6 meV) than for COF-TAPB-BT (78.0 meV), suggesting more favorable exciton dissociation in COF-PY-BT. Time-resolved PL measurements further showed that COF-PY-BT exhibited the longest excited-state lifetime of 1.41 ns, compared with 1.23 ns for COF-TAPB-BT and 1.18 ns for COF-ETTA-BT (Figure 2c).

Time-dependent density functional theory (TD-DFT) calculations revealed pronounced differences in local photoinduced charge separation. COF-PY-BT exhibited the largest electron-hole spatial separation among the three frameworks (Figures 2a,b and S14).[53,54] Molecular-orbital maps showed anisotropic separation of the highest occupied and lowest unoccupied orbitals along the diagonal direction of the rhombic pore (Figure S15), indicating a directional local photoinduced response. Excited-state dipole analysis of a representative COF-PY-BT donor−acceptor fragment further supported the directional character of this local charge redistribution (Figure S16). Complementary band-structure calculations showed more dispersive bands near the Fermi level for COF-PY-BT, suggesting more favorable carrier transport and charge redistribution (Figure 2d−f).[55,56]

Light-induced surface-charge redistribution was examined by photo-assisted Kelvin probe force microscopy (KPFM). Under the same measurement configuration, all three membranes exhibited negative surface photovoltage signals, but with substantially different magnitudes. COF-PY-BT showed the largest SPV of −137.7 mV, compared with −92.5 mV for COF-ETTA-BT and −89.0 mV for COF-TAPB-BT (Figure

https://doi.org/10.1021/jacs.6c10380
J. Am. Chem. Soc. 2026, 148, 38932−38940

Downloaded from pubs.acs.org/jacsat/article-pdf/148/36/38932/6810152/jacs.6c10380.pdf by UNIV OF NORTH TEXAS user on 26 September 2026

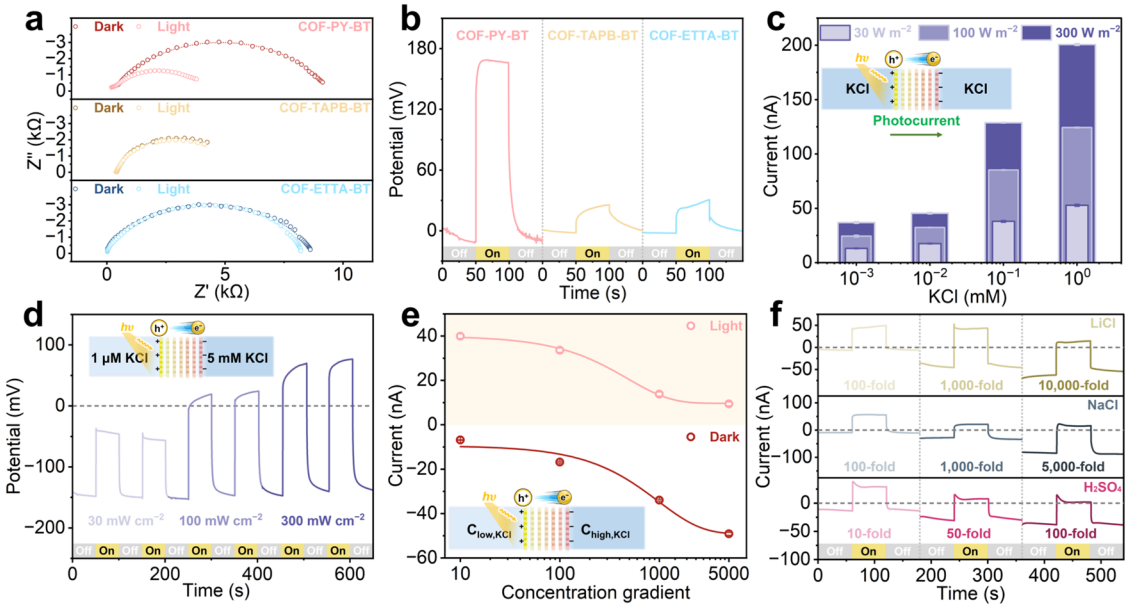


Figure 3. Light-induced transmembrane bias and active ion pumping against chemical gradients. (a) Nyquist plots of COF-PY-BT, COF-TAPB-BT, and COF-ETTA-BT recorded in the dark and under illumination in a membrane-separated electrochemical cell. (b) Transmembrane photovoltage of the three membranes in a symmetric cell containing 1.0 μM KCl on both sides under xenon-lamp illumination (300 mW cm^{-2}). (c) Zero-bias photocurrent of COF-PY-BT as a function of light intensity and KCl concentration under symmetric conditions. Error bars represent the standard deviation of three independent measurements. (d) Zero-current potential of COF-PY-BT under periodic illumination across a 5,000-fold KCl gradient (1.0 μM‖5.0 mM). (e) Zero-bias current of COF-PY-BT across KCl gradients ranging from 50-fold to 5,000-fold in the dark and under illumination. (f) Zero-bias current responses of COF-PY-BT across NaCl, LiCl, and H_2SO_4 gradients, with the low-concentration side fixed at 1.0 μM.

2g–i). At the periodic-framework level, dipolar retention and cancellation were evaluated using Berry-phase calculations based on the complete structural models. Within the reported Berry-phase branch, COF-PY-BT retains a pronounced nonzero periodic dipolar component of approximately 3.03 D, COF-TAPB-BT shows nearly complete cancellation, and COF-ETTA-BT retains a finite component of approximately 1.95 D. These calculations reveal framework-dependent differences in the retention and cancellation of periodic dipolar components, consistent with a role of lattice symmetry in modulating the periodic dipolar response (Figure S17).

2.3. Light-Induced Transmembrane Response and Active Ion Transport

We next used electrochemical impedance spectroscopy (EIS) to probe illumination-induced changes in the membrane-separated electrochemical cell. Upon illumination, the Nyquist semicircle of COF-PY-BT contracted markedly, with the fitted apparent polarization resistance decreasing from 9.09 to 4.20 kΩ. By comparison, COF-TAPB-BT showed only a modest decrease from 5.18 to 4.81 kΩ, whereas COF-ETTA-BT exhibited minimal change from 8.80 to 8.48 kΩ (Figure 3a and Schemes S4 and S5). Because the measured impedance contains contributions from the electrodes, electrolytes, membrane, and membrane/electrolyte interfaces, the fitted resistance reflects the composite polarization response of the complete cell and cannot be assigned solely to the COF membrane. The substantially larger light-induced change observed for COF-PY-BT indicates a stronger perturbation of the overall cell polarization response upon illumination.

We then directly examined the membrane-scale photoresponse in a symmetric two-compartment cell containing identical KCl solutions on both sides, thereby removing an externally imposed concentration gradient. KCl was selected because the similar bulk mobilities of K^+ and Cl^- minimize contributions from ion-mobility mismatch. Under xenon-lamp illumination, COF-PY-BT generated a transmembrane photovoltage of 177 mV in 1.0 μM KCl, substantially larger than those of COF-ETTA-BT (32 mV) and COF-TAPB-BT (28 mV) (Figure 3b). Control experiments using the electrolyte alone or a non-photoactive polyacrylonitrile (PAN) membrane produced negligible signals under the same conditions (Figure S18), supporting assignment of the observed response to the photoactive COF membrane.

The photocurrent rose rapidly upon illumination and returned to baseline in the dark over repeated light on–off cycles, demonstrating a reversible response. Possible thermal contributions were evaluated by monitoring the temperature near the electrode surfaces during continuous illumination. Even at a higher light intensity of 500 mW cm^{-2} for 1.5 h, the temperature change remained below 0.5 °C, making a dominant photothermal contribution to the observed electrical response unlikely. The photocurrent increased with both light intensity and electrolyte concentration (Figures 3c and S19), demonstrating that the membrane-scale response depends on the excitation conditions and the availability of mobile ions. Under otherwise identical conditions, COF-PY-BT generated photocurrents approximately five and nine times greater than those of COF-ETTA-BT and COF-TAPB-BT, respectively (Figures S20–S22). In all three COF membranes, the photocurrent polarity was consistent with net cation transport from the illuminated toward the non-illuminated compartment.

To determine what defines the direction of the membrane-scale response, we independently varied the membrane orientation and illumination direction while keeping the electrode positions, electrical connections, electrolyte compo-

https://doi.org/10.1021/jacs.6c10380
J. Am. Chem. Soc. 2026, 148, 38932–38940

Downloaded from pubs.acs.org/jacsat/article-pdf/148/36/38932/6810152/jacs.6c10380.pdf by UNIV OF NORTH TEXAS user on 26 September 2026

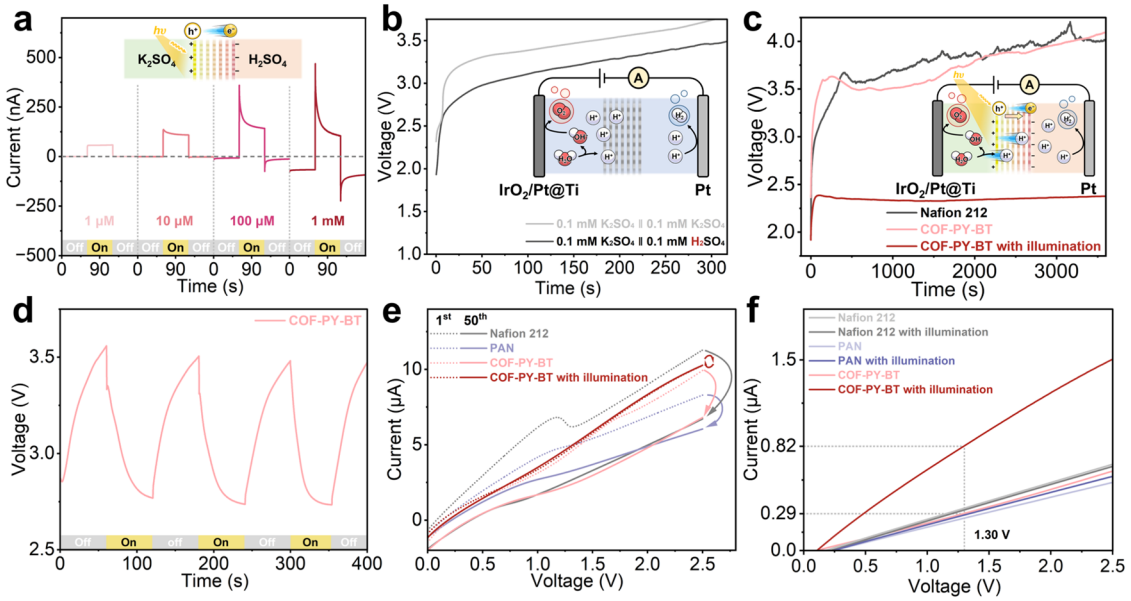


Figure 4. Light-regulated proton microenvironments during electrolysis. (a) Zero-bias current responses across COF-PY-BT in matched-concentration K_2SO_4‖H_2SO_4 electrolytes (1.0 μM−1.0 mM) under dark and illuminated conditions. (b) Galvanostatic full-cell voltage at 10 μA for different electrolyte configurations separated by Nafion 212. The inset shows the cell configuration. (c) Full-cell voltage of electrolyzers assembled with different membranes in 0.1 mM K_2SO_4‖0.1 mM H_2SO_4 at 10 μA. (d) Full-cell voltage response of the COF-PY-BT electrolyzer under periodically modulated illumination. (e) Cyclic voltammograms of electrolyzers assembled with different membranes. Dashed and solid traces denote the 1st and 50th cycles, respectively. (f) Polarization curves of electrolyzers assembled with different membranes in pure water under dark and illuminated conditions. Unless otherwise noted, illumination was provided by a xenon lamp at 300 mW cm^{-2}.

sition, incident light intensity, illuminated area, and cell geometry unchanged. Across the four configurations, reversing the illumination direction reversed the zero-bias photocurrent polarity for both membrane orientations, whereas flipping the membrane while maintaining the same illumination direction preserved the corresponding polarity (Figure S23). These crossed-control measurements demonstrate that the polarity of the macroscopic through-plane response follows the illumination direction rather than the identity of the illuminated membrane surface.

Based on these experimental observations, we propose that one-sided illumination creates an asymmetric excitation condition across the membrane thickness, under which carrier transport, trapping, recombination, and interfacial charge redistribution may lead to unequal charge accumulation at the two membrane/electrolyte interfaces and thereby generate the observed transmembrane bias. The detailed microscopic carrier-transfer process linking the local photoresponse to the membrane-scale electrical asymmetry remains to be directly resolved (Figure S24).

2.4. Active Ion Pumping against Chemical Gradients

Having established a directional light-induced transmembrane response under symmetric electrolyte conditions, we next examined whether it could oppose an imposed chemical-potential gradient. A KCl concentration gradient was applied across the membrane, with illumination directed from the low-concentration side toward the high-concentration side. In the dark, all three membranes exhibited a diffusion-driven zero-bias current associated with passive ion transport down the concentration gradient. Upon illumination, the current shifted progressively in the light-driven direction and ultimately crossed zero with increasing light intensity, demonstrating that the light-induced transmembrane bias counteracted and eventually exceeded the chemical driving force.

The extent of current inversion differed markedly among the three membranes. COF-PY-BT sustained current reversal across a 5,000-fold KCl gradient (Figure 3d,e), whereas COF-TAPB-BT and COF-ETTA-BT showed reversal only under gradients of approximately 50-fold (Figures S25−S27). Because the pore apertures of all three COFs exceed the hydrated diameters of the tested ions,[57] and their accessible surface areas differ by substantially less than their pumping performances, passive pore-size and surface-area differences alone are unlikely to account for the observed disparity in active transport.

The pumping response of COF-PY-BT was stable and reversible over repeated illumination cycles, with rapid recovery in the dark and no detectable loss of response. To examine whether this behavior extended beyond KCl, we further tested NaCl, LiCl, and H_2SO_4 electrolytes. COF-PY-BT exhibited clear current inversion in all these systems, sustaining uphill transport across concentration gradients of up to 5,000-fold for NaCl, 10,000-fold for LiCl, and 100-fold for H_2SO_4 (Figure 3f). These results demonstrate that the light-driven pumping response is not limited to a single electrolyte. The particularly large sustainable gradient observed for LiCl may partly reflect the lower mobility of Li^+, which can reduce passive back-diffusion and thereby increase the relative contribution of the light-induced driving force (Figures S28 and S29).[58] The resulting active-transport performance is summarized in Table S4.

To assess the energetic consistency of this current inversion, we compared the measured light-induced potential response with the Nernst potential associated with the imposed concentration gradient

$$\Delta E = \frac{k_B T}{e} \ln\left(\frac{c_{high}}{c_{low}}\right)$$

https://doi.org/10.1021/jacs.6c10380
J. Am. Chem. Soc. 2026, 148, 38932−38940

Downloaded from pubs.acs.org/jacsat/article-pdf/148/36/38932/6810152/jacs.6c10380.pdf by UNIV OF NORTH TEXAS user on 26 September 2026

where ΔE is the equilibrium potential difference, k_B is the Boltzmann constant, T is the temperature, e is the elementary charge, and c_{high} and c_{low} are the KCl concentrations in the two reservoirs. For a 5,000-fold concentration ratio of monovalent ions at room temperature, the corresponding Nernst potential is approximately 218 mV. Under the same gradient, COF-PY-BT generated a light-induced transmembrane potential response of 213 mV (Figure 3d). The near equivalence of these values indicates that the light-induced electrical bias is of sufficient magnitude to compensate the electrochemical potential associated with the imposed concentration gradient, consistent with the observed current inversion. By comparison, COF-TAPB-BT and COF-ETTA-BT generated substantially smaller light-induced potentials of 33 and 46 mV, respectively, both below the approximately 118 mV Nernst potential associated with a 100-fold monovalent concentration gradient. Their smaller potential responses are consistent with the more limited current inversion observed for these membranes (Figures S30 and S31).

2.5. Operando Regulation of Proton Microenvironments during Electrolysis

Building on the uphill ion-pumping results, we next investigated light-driven regulation of proton distributions under conditions relevant to electrolysis. We first tested COF-PY-BT in a symmetric two-compartment cell containing identical 0.1 mM HCl solutions on both sides. Illumination generated reproducible zero-bias current responses, demonstrating a directional transmembrane electrical response in the absence of a pre-existing proton-activity gradient (Figure S32).

We then tested the ability of the light-induced response to oppose proton back-diffusion and maintain an initially imposed transmembrane proton-activity difference. Matched nominal concentrations of H_2SO_4 and K_2SO_4, ranging from 1.0 μM to 1.0 mM and corresponding to initial bulk ΔpH values of 1.3−4.3, were placed in the two compartments. The use of sulfate-based electrolytes on both sides minimized differences arising from anion chemistry while establishing an acidic-to-near-neutral proton-activity contrast. The membrane was illuminated from the K_2SO_4 side toward the H_2SO_4 side. In the dark, the higher mobility of H^+ relative to K^+ contributed to a net diffusion-driven current from the acidic compartment toward the near-neutral compartment.[59,60] Upon illumination, this current was strongly suppressed and subsequently reversed, indicating that the light-induced transmembrane bias counteracted the diffusion-driven ionic flux associated with the imposed proton-activity difference (Figure 4a). The response remained rapid and reversible over repeated light on−off cycles (Figures S33 and S34).

To probe light-induced changes in proton availability near the membrane surface, we performed scanning electrochemical microscopy (SECM) probe-approach-curve measurements using the proton-coupled reduction of 1,4-benzoquinone at a Pt ultramicroelectrode. Because this reaction consumes protons, the cathodic tip current provides a proton-sensitive electrochemical signal during the UME approach toward the membrane. For COF-PY-BT, illumination decreased the magnitude of the cathodic tip current relative to the dark condition, consistent with lower proton availability in the near-surface region. By contrast, the dark and illuminated approach curves of Nafion 212 remained much more closely overlapped (Figure S35).

The functional impact of this membrane-mediated proton regulation was then evaluated by integrating COF-PY-BT as the separator in a two-compartment water electrolyzer (Figure S36). The anodic and cathodic compartments contained K_2SO_4 and H_2SO_4, respectively, at matched nominal concentrations of 0.1 or 1.0 mM, establishing distinct proton environments while maintaining a common sulfate-based electrolyte chemistry. The full-cell voltage was used as a comparative operando readout of the cell-level consequences of light-regulated transmembrane proton and ion transport.

Control measurements with Nafion 212 first established the influence of electrolyte configuration on the full-cell voltage (Figures 4b and S37). Under galvanostatic electrolysis at 10 μA in 0.1 mM K_2SO_4‖0.1 mM H_2SO_4 and at 100 μA in 1.0 mM K_2SO_4‖1.0 mM H_2SO_4, illumination caused an immediate decrease in the apparent full-cell voltage (Figures 4c and S38). Under the 0.1 mM proof-of-concept condition, the decrease was approximately 45%. Periodic modulation of the illumination produced corresponding reversible changes in the full-cell voltage (Figure 4d). The rapid onset is consistent with a prompt light-induced membrane response, whereas the subsequent relaxation toward steady state is consistent with electrolyte redistribution and the establishment of a new steady-state ion distribution between the compartments. EIS measurements under the 0.1 mM K_2SO_4‖0.1 mM H_2SO_4 condition showed that the uncompensated resistance changed only slightly from 57.0 kΩ in the dark to 56.7 kΩ under illumination. At 10 μA, this resistance change corresponds to only approximately 3 mV of the total light-induced apparent full-cell voltage decrease of 1.72 V. The voltage response is therefore not dominated by the change in uncompensated resistance and is consistent with membrane-mediated proton/ion redistribution and modulation of concentration polarization.

Illumination also improved the voltage stability under asymmetric electrolyte conditions. After reaching steady state within approximately 120 s, the illuminated COF-PY-BT device exhibited voltage fluctuations below ±1%, whereas devices incorporating control membranes showed progressive voltage increases over the same period (Figures 4c and S37). In the 1.0 mM K_2SO_4‖1.0 mM H_2SO_4 configuration, operando bulk-pH measurements showed that the anodic compartment remained near neutral at pH 7.0, while the cathodic compartment remained acidic at pH 2.4, corresponding to a bulk ΔpH of 4.6. This persistent bulk pH contrast supports the maintenance of the initially imposed transmembrane proton-activity difference during electrochemical operation.

Electrochemical cycling showed a similar trend. Under illumination, cyclic voltammetry exhibited less than 1% current decay over 50 cycles, whereas measurements in the dark and devices incorporating Nafion 212 or PAN membranes showed more pronounced current decay (Figures 4d,e and S39−S41). In situ FT-IR measurements under different proton-activity conditions showed no pronounced or systematic changes in the C═N-associated region, providing no spectroscopic evidence for strong or persistent bulk protonation of the imine framework (Figure S42). Consistently, post-electrolysis FT-IR and N 1s XPS spectra showed no pronounced changes attributable to persistent protonation (Figure S43), while post-cycling characterization confirmed that the membrane retained its structural integrity and crystallinity (Figure S44).

We further examined the active-separation response at elevated electrolyte concentration and current density. In 0.1

Downloaded from pubs.acs.org/jacsat/article-pdf/148/36/38932/6810152/jacs.6c10380.pdf by UNIV OF NORTH TEXAS user on 26 September 2026

https://doi.org/10.1021/jacs.6c10380
J. Am. Chem. Soc. 2026, 148, 38932−38940

M K_2SO_4||0.1 M H_2SO_4, illumination decreased the apparent full-cell voltage by approximately 90 mV at 10 mA cm^{-2} (Figure S45). The polarization curves were recorded in a two-electrode configuration, and the applied voltage represents the full-cell voltage between the IrO_2/Pt@Ti anode and Pt cathode. The measured change in uncompensated resistance would contribute only approximately 6.4 mV to this voltage decrease, leaving a residual decrease of approximately 83.6 mV after subtracting the estimated ohmic contribution. Gas evolution at both electrodes and the absence of obvious short-circuit behavior supported the assignment of the measured current to water electrolysis. Light-induced full-cell voltage modulation therefore remained detectable at the hundred-millimolar electrolyte level, with the residual response consistent with light-regulated transmembrane proton/ion redistribution and modulation of concentration polarization at the membrane interfaces.

Electrolysis was also evaluated in pure water, where proton availability is intrinsically limited. At an applied full-cell voltage of 1.30 V, devices incorporating COF-PY-BT, Nafion 212, and PAN exhibited comparable dark currents. Upon illumination, the current of the COF-PY-BT device increased from approximately 0.29 to 0.82 μA, corresponding to a 2.8-fold enhancement, whereas only minor changes were observed for the Nafion 212 and PAN controls (Figure 4f).

3. CONCLUSION

Biological systems exploit chemical asymmetry to organize reactions that are difficult to sustain in homogeneous environments. Here, we show that COF-PY-BT combines pronounced local photoinduced charge separation with a strong light-induced transmembrane electrical response under one-sided illumination. Periodic Berry-phase calculations reveal framework-dependent differences in the retention and cancellation of dipolar components, while crossed-control experiments establish that the direction of the membrane-scale response follows the illumination direction. The resulting transmembrane bias counteracts diffusion-driven equilibration and enables uphill proton and ion transport, helping sustain distinct proton activities across the membrane. When integrated as an active separator in a two-compartment water electrolyzer, COF-PY-BT helps maintain distinct anodic and cathodic proton environments, lowers the apparent full-cell voltage, and improves voltage stability under proof-of-concept operating conditions. These cell-level responses are consistent with membrane-mediated ion redistribution and modulation of concentration polarization.

More broadly, this work distinguishes the roles of local electronic structure, periodic framework organization, and asymmetric illumination in light-driven active membrane transport. Framework symmetry modulates the retention of periodic dipolar components, whereas one-sided illumination defines the direction of the macroscopic transmembrane response. Although the microscopic carrier-transfer pathway connecting local excitation to membrane-scale electrical asymmetry remains unresolved, the resulting light-induced bias provides an active means of sustaining nonequilibrium proton distributions against passive diffusion. Light-driven active separation therefore offers a general strategy for dynamically regulating electrochemical microenvironments in aqueous systems.

■ ASSOCIATED CONTENT

Supporting Information

The Supporting Information is available free of charge at https://pubs.acs.org/doi/10.1021/jacs.6c10380.

Experimental procedures, materials and characterization methods, digital photographs of the membranes, cross-sectional SEM images, HR-TEM images, AFM topographic images, FT-IR spectra, pore-size distributions, XRD patterns, ^{13}C NMR spectra, SHG spectra, SECM probe-approach curves, XPS spectra, and electrochemical test results (PDF)

■ AUTHOR INFORMATION

Corresponding Author

Qi Sun − *Key Laboratory of Biomass Chemical Engineering of Ministry of Education, College of Chemical and Biological Engineering, Zhejiang University, Hangzhou 310027, China;* orcid.org/0000-0002-1698-8741; Email: sunqichs@zju.edu.cn

Authors

Zhuozhi Lai − *Key Laboratory of Biomass Chemical Engineering of Ministry of Education, College of Chemical and Biological Engineering, Zhejiang University, Hangzhou 310027, China*

Zhiwei Xing − *Key Laboratory of Biomass Chemical Engineering of Ministry of Education, College of Chemical and Biological Engineering, Zhejiang University, Hangzhou 310027, China*

Yongxin Ge − *State Key Laboratory of Catalysis, Dalian Institute of Chemical Physics, Chinese Academy of Sciences, Dalian 116023, China; University of Chinese Academy of Sciences, Beijing 100049, China*

Jiaming Yi − *Key Laboratory of Biomass Chemical Engineering of Ministry of Education, College of Chemical and Biological Engineering, Zhejiang University, Hangzhou 310027, China*

Sai Wang − *Hangzhou Institute of Advanced Studies, Zhejiang Normal University, Hangzhou 310015, China*

Ruotian Chen − *State Key Laboratory of Catalysis, Dalian Institute of Chemical Physics, Chinese Academy of Sciences, Dalian 116023, China*

Shengqian Ma − *Department of Chemistry, University of North Texas, Denton, Texas 76201, United States;* orcid.org/0000-0002-1897-7069

Complete contact information is available at: https://pubs.acs.org/10.1021/jacs.6c10380

Author Contributions

The manuscript was written through contributions of all authors. All authors have given approval to the final version of the manuscript.

Notes

The authors declare no competing financial interest.

■ ACKNOWLEDGMENTS

This work was funded by the National Key Research and Development Program of China (2024YFB3815700) and the National Natural Science Foundation of China (22421004 and 22578386). We would like to express our gratitude to Y.G. and R.C. from the Dalian Institute of Chemical Physics, Chinese

Downloaded from pubs.acs.org/jacsat/article-pdf/148/36/38932/6810152/jacs.6c10380.pdf by UNIV OF NORTH TEXAS user on 26 September 2026

Academy of Sciences, for their assistance with surface photovoltage microscopy measurements. We also extend our thanks to F. Chen and Y. Qiu from the Analytical Testing Center of the Department of Chemistry at Zhejiang University for conducting SEM and GIWAXS measurements.

REFERENCES

(1) Li, H.; Li, H.; Wei, P.; Wang, Y.; Zang, Y.; Gao, D.; Wang, G.; Bao, X. Tailoring acidic microenvironments for carbon-efficient CO_2 electrolysis over a Ni−N−C catalyst in a membrane electrode assembly electrolyzer. *Energy Environ. Sci.* **2023**, *16*, 1502−1510.
(2) Peng, S. *Electrochemical Hydrogen Production from Water Splitting: Basic, Materials, and Progress*; Springer: Singapore, 2023 DOI: 10.1007/978-981-99-4468-2.
(3) Song, Y.; Musgrave, C. B.; Su, J.; Huang, L.; Guo, W.; Liu, Y.; Li, G.; Xin, Y.; Zhang, Q.; Feng, X.; Liao, C.; Liu, S.; Kwok, R. T. K.; Lam, J. W. Y.; He, M.; Choong, K. S.; Feng, Z.; Tang, B. Z.; Goddard, W. A.; Ye, R. Efficient CO_2-to-methanol electrocatalysis in acidic media via microenvironment-tuned cobalt phthalocyanine. *Nat. Nanotechnol.* **2026**, *21*, 78−86.
(4) Huang, J.; Borca, C. N.; Huthwelker, T.; Yüzbasi, N. S.; Baster, D.; El Kazzi, M.; Schneider, C. W.; Schmidt, T. J.; Fabbri, E. Surface oxidation/spin state determines oxygen evolution reaction activity of cobalt-based catalysts in acidic environment. *Nat. Commun.* **2024**, *15*, No. 3067.
(5) Rong, C.; Dastafkan, K.; Wang, Y.; Zhao, C. Breaking the activity and stability bottlenecks of electrocatalysts for oxygen evolution reactions in acids. *Adv. Mater.* **2023**, *35*, No. 2211884.
(6) Wan, C.; Zhang, Z.; Dong, J.; Xu, M.; Pu, H.; Baumann, D.; Lin, Z.; Wang, S.; Huang, J.; Shah, A. H.; Pan, X.; Hu, T.; Alexandrova, A. N.; Huang, Y.; Duan, X. Amorphous nickel hydroxide shell tailors local chemical environment on platinum surface for alkaline hydrogen evolution reaction. *Nat. Mater.* **2023**, *22*, 1022−1029.
(7) Oener, S. Z.; Foster, M. J.; Boettcher, S. W. Accelerating water dissociation in bipolar membranes and for electrocatalysis. *Science* **2020**, *369*, 1099−1103.
(8) Tong, W.; Forster, M.; Dionigi, F.; Dresp, S.; Sadeghi Erami, R.; Strasser, P.; Cowan, A. J.; Farràs, P. Electrolysis of low-grade and saline surface water. *Nat. Energy* **2020**, *5*, 367−377.
(9) Cordes, M.; Giese, B. Electron transfer in peptides and proteins. *Chem. Soc. Rev.* **2009**, *38*, 892−901.
(10) Lee, K. Y.; Park, S.-J.; Lee, K. A.; Kim, S.-H.; Kim, H.; Meroz, Y.; Mahadevan, L.; Jung, K.-H.; Ahn, T. K.; Parker, K. K.; Shin, K. Photosynthetic artificial organelles sustain and control ATP-dependent reactions in a protocellular system. *Nat. Biotechnol.* **2018**, *36*, 530−535.
(11) Mous, S.; Gotthard, G.; Ehrenberg, D.; Sen, S.; Weinert, T.; Johnson, P. J. M.; James, D.; Nass, K.; Furrer, A.; Kekilli, D.; Ma, P.; Brünle, S.; Casadei, C. M.; Martiel, I.; Dworkowski, F.; Gashi, D.; Skopintsev, P.; Wranik, M.; Knopp, G.; Panepucci, E.; Panneels, V.; Cirelli, C.; Ozerov, D.; Schertler, G. F. X.; Wang, M.; Milne, C.; Standfuss, J.; Schapiro, I.; Heberle, J.; Nogly, P. Dynamics and mechanism of a light-driven chloride pump. *Science* **2022**, *375*, 845−851.
(12) Shao, B.; Fu, H.; Aprahamian, I. A molecular anion pump. *Science* **2024**, *385*, 544−549.
(13) Steinberg-Yfrach, G.; Liddell, P. A.; Hung, S.-C.; Moore, A. L.; Gust, D.; Moore, T. A. Conversion of light energy to proton potential in liposomes by artificial photosynthetic reaction centres. *Nature* **1997**, *385*, 239−241.
(14) Xie, X.; Crespo, G. A.; Mistlberger, G.; Bakker, E. Photocurrent generation based on a light-driven proton pump in an artificial liquid membrane. *Nat. Chem.* **2014**, *6*, 202−207.
(15) Xiao, K.; Chen, L.; Chen, R.; Heil, T.; Lemus, S. D. C.; Fan, F.; Wen, L.; Jiang, L.; Antonietti, M. Artificial light-driven ion pump for photoelectric energy conversion. *Nat. Commun.* **2019**, *10*, No. 74.
(16) Li, C.; Zhai, Y.; Jiang, H.; Li, S.; Liu, P.; Gao, L.; Jiang, L. Bioinspired light-driven chloride pump with helical porphyrin channels. *Nat. Commun.* **2024**, *15*, No. 832.
(17) Xiao, K.; Jiang, L.; Antonietti, M. Ion transport in nanofluidic devices for energy harvesting. *Joule* **2019**, *3*, 2364−2380.
(18) Nie, X.; Hu, Z.; Xiao, T.; Li, L.; Jin, J.; Liu, K.; Liu, Z. Light-powered ion pumping in a cation-selective conducting polymer membrane. *Angew. Chem., Int. Ed.* **2022**, *61*, No. e202201138.
(19) Zhang, Z.; Kong, X.-Y.; Xie, G.; Li, P.; Xiao, K.; Wen, L.; Jiang, L. "Uphill" cation transport: A bioinspired photo-driven ion pump. *Sci. Adv.* **2016**, *2*, No. e1600689.
(20) Xu, L.; Zhao, B.; Liu, W.; Zhang, J.; Zhang, X.; Zaker, S. S. M. A.; Lin, S. Flow-synchronized ring-shaped electrochemical ion pumping for redox-free desalination without terminal electrodes. *Nat. Chem. Eng.* **2026**, *3*, 100−111.
(21) Kautz, R.; Herman, A.; Heffernan, E. J.; Shushan Alshochat, K.; Grossman, E.; Saxena, R.; Muñetón, C.; Larson, D.; Ager, J. W.; Toma, F. M.; Ardo, S.; Segev, G. A nanoporous capacitive electrochemical ratchet for continuous ion separations. *Nat. Mater.* **2026**, *25*, 1037−1044.
(22) Liu, W.; Dykstra, J. E.; Biesheuvel, P. M.; Xu, L.; Lin, S. Theory for dynamic ion transport in ion-shuttling electrodes for electrochemical ion pumping. *Nat. Water* **2025**, *3*, 1025−1037.
(23) Lu, M.; Zhang, S.-B.; Li, R.-H.; Dong, L.-Z.; Yang, M.-Y.; Huang, P.; Liu, Y.-F.; Li, Z.-H.; Zhang, H.; Zhang, M.; Li, S.-L.; Lan, Y.-Q. 3D covalent organic frameworks with 16-connectivity for photocatalytic $C(sp^3)-C(sp^2)$ cross-coupling. *J. Am. Chem. Soc.* **2024**, *146*, 25832−25840.
(24) Gu, X.; Niu, H.; Shi, Y.; Ding, H.; Cai, Y.; Jiang, G. Cross-shaped donor-π-acceptor covalent organic frameworks with tunable push-pull architectures for effective photocatalytic H_2O_2 production. *Angew. Chem., Int. Ed.* **2026**, *65*, No. e20491.
(25) Liu, R.; Zhao, D.; Ji, S.; Shao, H.; Chen, Y.; Feng, M.; Wang, T.; Li, J.; Lin, M.; Sum, T. C.; Yan, N.; Seki, S.; Jiang, D. Harvesting singlet and triplet excitation energies in covalent organic frameworks for highly efficient photocatalysis. *Nat. Mater.* **2025**, *24*, 1245−1257.
(26) Joshi, T.; Chen, C.; Li, H.; Diercks, C. S.; Wang, G.; Waller, P. J.; Li, H.; Bredas, J.-L.; Yaghi, O. M.; Crommie, M. F. Local electronic structure of molecular heterojunctions in a single-layer 2D covalent organic framework. *Adv. Mater.* **2019**, *31*, No. 1805941.
(27) Chen, Y.; Xue, Y.; Xu, X.; Su, Y.; Tong, X.; Zhu, L.; Zuo, Y.; Ban, C.; Chen, J.; Que, W.; Zheng, Y.; Guo, W. Tetrazine-enhanced donor-acceptor-donor metal-organic frameworks for photodynamic antibacterial therapy and wound healing. *Nat. Commun.* **2025**, *16*, No. 10508.
(28) Yang, H.; Hao, M.; Xie, Y.; Liu, X.; Liu, Y.; Chen, Z.; Wang, X.; Waterhouse, G. I. N.; Ma, S. Tuning local charge distribution in multicomponent covalent organic frameworks for dramatically enhanced photocatalytic uranium extraction. *Angew. Chem., Int. Ed.* **2023**, *62*, No. e202303129.
(29) Zhao, X.; Pachfule, P.; Thomas, A. Covalent organic frameworks (COFs) for electrochemical applications. *Chem. Soc. Rev.* **2021**, *50*, 6871−6913.
(30) Zhang, L.; Du, J.; Xie, Z.; Chen, L.; Li, W.; Geng, W.; Zhou, Y.; Ou, X.; Gong, C.; Gao, Y.; He, S.; Yan, C.; Zhao, C.; Jiao, Y.; Yang, S.-Y.; Huang, B.; Lam, J. W. Y.; Qian, J.; Jiang, J.; Tang, B. Z.; Deng, H. Discovery of highly fluorescent covalent organic frameworks through AI-assisted iterative experiment-learning cycles. *Nat. Chem.* **2025**, *17*, 1645−1654.
(31) Sun, K.; Huang, Y.; Sun, F.; Wang, Q.; Zhou, Y.; Wang, J.; Zhang, Q.; Zheng, X.; Fan, F.; Luo, Y.; Jiang, J.; Jiang, H.-L. Dynamic structural twist in metal-organic frameworks enhances solar overall water splitting. *Nat. Chem.* **2024**, *16*, 1638−1646.
(32) Hu, H.; Wang, Z.; Cao, L.; Zeng, L.; Zhang, C.; Lin, W.; Wang, C. Metal-organic frameworks embedded in a liposome facilitate overall photocatalytic water splitting. *Nat. Chem.* **2021**, *13*, 358−366.
(33) Blätte, D.; Ortmann, F.; Bein, T. Photons, excitons, and electrons in covalent organic frameworks. *J. Am. Chem. Soc.* **2024**, *146*, 32161−32205.

Downloaded from pubs.acs.org/jacsat/article-pdf/148/36/38932/6810152/jacs.6c10380.pdf by UNIV OF NORTH TEXAS user on 26 September 2026

(34) Banerjee, T.; Podjaski, F.; Kröger, J.; Biswal, B. P.; Lotsch, B. V. Polymer photocatalysts for solar-to-chemical energy conversion. *Nat. Rev. Mater.* **2021**, *6*, 168−190.
(35) Diercks, C. S.; Yaghi, O. M. The atom, the molecule, and the covalent organic framework. *Science* **2017**, *355*, No. eaal1585.
(36) Pal, H.; Karmakar, A.; Sadhukhan, A.; Sharma, R. K.; Paul, S.; Addicoat, M. A.; Nishiyama, Y.; Pathak, B.; Kundu, S.; Banerjee, R. Cation-assisted water oxidation with crown ether-based covalent organic frameworks. *J. Am. Chem. Soc.* **2025**, *147*, 20406−20416.
(37) Hu, X.-F.; Jiang, T.; Fan, H.; Guan, Y.-F.; Chen, J.-J.; Yu, H.-Q.; Elimelech, M. Dual-regulated covalent organic framework membranes with near-theoretical pore sizes for angstrom-scale ion separations. *Sci. Adv.* **2025**, *11*, No. eady3587.
(38) Yang, Y.; Liang, B.; Kreie, J.; Hambsch, M.; Liang, Z.; Wang, C.; Huang, S.; Dong, X.; Gong, L.; Liang, C.; Lou, D.; Zhou, Z.; Lu, J.; Yang, Y.; Zhuang, X.; Qi, H.; Kaiser, U.; Mannsfeld, S. C. B.; Liu, W.; Gölzhäuser, A.; Zheng, Z. Elastic films of single-crystal two-dimensional covalent organic frameworks. *Nature* **2024**, *630*, 878−883.
(39) Li, J.; Liu, Q.; Shen, J.; Cao, L.; Cai, Y.; Zhou, W.; Zhang, H.; Zhang, X.; Han, Y.; Lai, Z. High-strength conjugated polymer framework membranes for ultrafast and precise separations. *Nat. Sustain.* **2026**, *9*, 271−282.
(40) Zhan, G.; Koek, B.; Yuan, Y.; Liu, Y.; Mishra, V.; Lenzi, V.; Strutyński, K.; Li, C.; Zhang, R.; Zhou, X.; Choi, H. S.; Cai, Z.-F.; Almarza, J.; Mali, K. S.; Mateo-Alonso, A.; Franco, M. M.; Zhu, Y.; De Feyter, S.; Loh, K. P. Moiré two-dimensional covalent organic framework superlattices. *Nat. Chem.* **2025**, *17*, 518−524.
(41) Hu, Y.; Sengupta, B.; Long, H.; Wayment, L. J.; Ciora, R.; Jin, Y.; Wu, J.; Lei, Z.; Friedman, K.; Chen, H.; Yu, M.; Zhang, W. Molecular recognition with resolution below 0.2 angstroms through thermoregulatory oscillations in covalent organic frameworks. *Science* **2024**, *384*, 1441−1447.
(42) Dong, J.; Zhao, D. Porous and permutable peptide frameworks. *Nat. Chem.* **2022**, *14*, 852−854.
(43) Yuan, J.; Mai, Z.; Parkinson, M.; Zhou, Y.; Hou, J.; Cao, X.; Sun, S.-P.; Zhang, Y.; Zhu, J.; Elimelech, M. Precision-engineered crystalline covalent organic framework membranes with staggered ABC stacking for high-performance desalination. *J. Am. Chem. Soc.* **2025**, *147*, 47477−47488.
(44) Zhang, W.; Chen, L.; Dai, S.; Zhao, C.; Ma, C.; Wei, L.; Zhu, M.; Chong, S. Y.; Yang, H.; Liu, L.; Bai, Y.; Yu, M.; Xu, Y.; Zhu, X.-W.; Zhu, Q.; An, S.; Sprick, R. S.; Little, M. A.; Wu, X.; Jiang, S.; Wu, Y.; Zhang, Y.-B.; Tian, H.; Zhu, W.-H.; Cooper, A. I. Reconstructed covalent organic frameworks. *Nature* **2022**, *604*, 72−79.
(45) Evans, A. M.; Parent, L. R.; Flanders, N. C.; Bisbey, R. P.; Vitaku, E.; Kirschner, M. S.; Schaller, R. D.; Chen, L. X.; Gianneschi, N. C.; Dichtel, W. R. Seeded growth of single-crystal two-dimensional covalent organic frameworks. *Science* **2018**, *361*, 52−57.
(46) Chang, J.; Zhang, Z.; Zheng, H.; Li, H.; Suo, J.; Ji, C.; Chen, F.; Zhang, S.; Wang, Z.; Valtchev, V.; Qiu, S.; Sun, J.; Fang, Q. Synthesis of three-dimensional covalent organic frameworks through a symmetry reduction strategy. *Nat. Chem.* **2025**, *17*, 571−581.
(47) Ghouse, S.; Guo, Z.; Gámez-Valenzuela, S.; Mücke, D.; Zhang, B.; Gao, L.; Paasch, S.; Fu, Y.; Huang, C.; Naisa, C.; Brunner, E.; Bonn, M.; Ruiz Delgado, M. C.; Sun, J.; Zou, R.; Kaiser, U.; Wang, M.; Feng, X. Towards single-crystalline two-dimensional poly(arylene vinylene) covalent organic frameworks. *Nat. Chem.* **2026**, *18*, 853−862.
(48) Zhao, J.; Wang, Y.; Zhu, Z.; Sun, Q.; Lyu, B.; Bie, M.; Hou, J.; Zhang, S.; Pan, F.; Jiang, Z. Ultrafast low-temperature pervaporation desalination with photo-responsive covalent organic framework membranes. *Nat. Water* **2025**, *3*, 1459−1467.
(49) Zhang, Y.; Wang, H.; Wang, W.; Zhou, Z.; Huang, J.; Yang, F.; Bai, Y.; Sun, P.; Ma, J.; Peng, L. E.; Tang, C. Y.; Shao, L. Engineering covalent organic framework membranes for efficient ionic/molecular separations. *Matter* **2024**, *7*, 1406−1439.
(50) Zhao, S.; Jiang, C.; Fan, J.; Hong, S.; Mei, P.; Yao, R.; Liu, Y.; Zhang, S.; Li, H.; Zhang, H.; Sun, C.; Guo, Z.; Shao, P.; Zhu, Y.; Zhang, J.; Guo, L.; Ma, Y.; Zhang, J.; Feng, X.; Wang, F.; Wu, H.; Wang, B. Hydrophilicity gradient in covalent organic frameworks for membrane distillation. *Nat. Mater.* **2021**, *20*, 1551−1558.
(51) Fu, G.; Yang, D.; Xu, S.; Li, S.; Zhao, Y.; Yang, H.; Wu, D.; Petkov, P. S.; Lan, Z.-A.; Wang, X.; Zhang, T. Construction of thiadiazole-bridged sp^2-carbon-conjugated covalent organic frameworks with diminished excitation binding energy toward superior photocatalysis. *J. Am. Chem. Soc.* **2024**, *146*, 1318−1325.
(52) Chen, D.-H.; Vankova, N.; Jha, G.; Yu, X.; Wang, Y.; Lin, L.; Kirschhöfer, F.; Greifenstein, R.; Redel, E.; Heine, T.; Wöll, C. Ultrastrong electron-phonon coupling in uranium-organic frameworks leading to inverse luminescence temperature dependence. *Angew. Chem., Int. Ed.* **2024**, *63*, No. e202318559.
(53) Qian, Y.; Han, Y.; Zhang, X.; Yang, G.; Zhang, G.; Jiang, H.-L. Computation-based regulation of excitonic effects in donor-acceptor covalent organic frameworks for enhanced photocatalysis. *Nat. Commun.* **2023**, *14*, No. 3083.
(54) Zhu, R.-M.; Liu, Y.; Han, W.-K.; Feng, J.-D.; He, Y.-O.; Pang, H.; Zhang, J.; Gu, Z.-G. Inwardly directed linker propagation: constructing 3D covalent organic frameworks for efficient H_2O_2 photosynthesis. *Angew. Chem., Int. Ed.* **2025**, *64*, No. e202510293.
(55) Thomas, S.; Li, H.; Zhong, C.; Matsumoto, M.; Dichtel, W. R.; Bredas, J.-L. Electronic structure of two-dimensional π-conjugated covalent organic frameworks. *Chem. Mater.* **2019**, *31*, 3051−3065.
(56) Wang, S.; Sun, Q.; Chen, W.; Tang, Y.; Aguila, B.; Pan, Y.; Zheng, A.; Yang, Z.; Wojtas, L.; Ma, S.; Xiao, F.-S. Programming covalent organic frameworks for photocatalysis: investigation of chemical and structural variations. *Matter* **2020**, *2*, 416−427.
(57) Zhao, Y.; Mamrol, N.; Tarpeh, W. A.; Yang, X.; Gao, C.; Van der Bruggen, B. Advanced ion transfer materials in electro-driven membrane processes for sustainable ion-resource extraction and recovery. *Prog. Mater. Sci.* **2022**, *128*, No. 100958.
(58) Cao, L.; Guo, W.; Ma, W.; Wang, L.; Xia, F.; Wang, S.; Wang, Y.; Jiang, L.; Zhu, D. Towards understanding the nanofluidic reverse electrodialysis system: well matched charge selectivity and ionic composition. *Energy Environ. Sci.* **2011**, *4*, 2259−2266.
(59) Sluyters, J. H.; Sluyters-Rehbach, M. Rotation of water molecules and its relation with the chemistry and physics of liquid water. *J. Phys. Chem. B* **2010**, *114*, 863−869.
(60) Gomez, A.; Thompson, W. H.; Laage, D. Neural-network-based molecular dynamics simulations reveal that proton transport in water is doubly gated by sequential hydrogen-bond exchange. *Nat. Chem.* **2024**, *16*, 1838−1844.

Downloaded from pubs.acs.org/jacsat/article-pdf/148/36/38932/6810152/jacs.6c10380.pdf by UNIV OF NORTH TEXAS user on 26 September 2026

https://doi.org/10.1021/jacs.6c10380
J. Am. Chem. Soc. 2026, 148, 38932−38940